

## Tailoring the transmittance of integrated optical waveguides with short metallic nanoparticle chains

Romain Quidant,<sup>1,2</sup> Christian Girard,<sup>3</sup> Jean-Claude Weeber,<sup>1</sup> and Alain Dereux<sup>1</sup>

<sup>1</sup>*Laboratoire de Physique de l'Université de Bourgogne, Optique Submicronique, 9 avenue A. Savary, F-21078 Dijon, France*

<sup>2</sup>*ICFO-Institut de Ciències Fotòniques, Jordi Girona 29, Nexus II, 08034 Barcelona, Spain*

<sup>3</sup>*CEMES, UPR-CNRS 8011, 29 Rue Jeanne Marvig, BP4347, F-31055 Toulouse, France*

(Received 17 September 2003; published 19 February 2004)

We study the ability of noble metal nanoparticle chains supporting localized surface plasmons to tailor the transmittance of channel waveguides on which they are deposited. The optical interaction between a micro-waveguide (MWG) and various arrangements of nanoparticles is first analyzed by means numerical calculations based on the Green's tensor formalism. For specific geometries of the particle chains, the transmission spectra of the composite device (MWG and nanoparticles) exhibits strong modulations in the optical range with the appearance of a neat band gap. The results of an experiment inspired by this theoretical study are also discussed. The photon scanning tunneling microscope images recorded over a MWG decorated with a short chain of gold nanoparticles for two different incident frequencies are found to be in qualitative agreement with the theoretical proposal.

DOI: 10.1103/PhysRevB.69.085407

PACS number(s): 73.20.Mf, 07.79.Fc, 78.66.Bz

### I. INTRODUCTION

Controlling light flows at the subwavelength scale might have significant practical applications for integrated optics devices miniaturization. Among the different routes explored to achieve this goal, surface plasmon polaritons (SPPs) sustained by noble metal nanostructures offers promising possibilities.<sup>1</sup> In this context, two different approaches can be distinguished.

(i) The first approach relies on SPP propagation along continuous systems such as thin metal stripes or nanowires. For these systems, the SPP propagation, i.e., the propagation of an electron density oscillations, can be directly used for optical signal transfer. Within this approach, plasmon propagation along metallic stripes with widths in the micrometer range have been investigated both theoretically<sup>2,3</sup> and experimentally.<sup>4-6</sup> More recently, in agreement with previous calculations,<sup>7</sup> Krenn *et al.* have reported experimental evidence for the propagation of near-infrared light along nanowires featuring subwavelength cross sections.<sup>8</sup>

(ii) The second approach of passive optical components miniaturization relying on SPP excitations exploits individual metallic nanoparticles arranged to form nanostructures such as chains or two dimensional arrays.<sup>9-11</sup> In this case, each individual nanoparticle rounds up the electron gas in the three dimensions and gives rise to "localized surface plasmons" (LSPs). These peculiar modes critically depend on the design of the nanoparticle.<sup>12</sup> The LSPs are also associated with a significant increase of both absorption and scattering phenomena.

Similarly to what happens with molecules,<sup>13</sup> the radiation efficiency of metallic nanoparticles is controlled by the local density of electromagnetic states available in the vicinity of the surroundings. For example, the LSP resonances are significantly shifted when the particles are located very close from a metallic surface sustaining SPP modes.<sup>14</sup> Changes of the effective polarizability also occur within ensembles of

nanoparticles via LSP-LSP coupling. When such nanoparticles are assembled to form a finite size chain, depending on the interparticle distances, two kinds of interaction can be identified. For closely packed particle arrays, the coupling implies essentially the evanescent fields that tails off each individual particles (evanescent coupling). Calculations performed by Quinten *et al.*<sup>15</sup> have shown that this kind of coupling could be optimized to promote the transfer of visible light through linear chains of silver nanoparticles with diameters typically scaled down to 30 nm. Very recently direct experimental evidence of this kind of short range coupling has been demonstrated by measuring electromagnetic energy transport along silver nanoparticle plasmon waveguides.<sup>16</sup>

For particles separated by distances greater than a few tenths of nanometers, the interaction relies on the interference of their scattered dipolar fields (dipole-dipole or far-field coupling). In this long range regime, a large two-dimensional (2D) periodic array of particles texturing a metallic film enables the creation a photonic band gap for the surface plasmon polariton mode sustained by the structure.<sup>17</sup> This effect has been used to propagate lightwaves along straight and bent lines of defects created into plasmonic crystals.<sup>18</sup>

SPPs are not the only way to control propagation of light in the coplanar geometry at the subwavelength scale. Indeed, an efficient light signal transfer can also be achieved using high optical index dielectric microwaveguides (MWGs) featuring submicrometre transverse cross-sections. When the lateral dimensions of the MWGs enter the subwavelength dimensions, recent experimental works recommend the use of optical evanescent fields instead of the common end-fire coupling to excite the input end of the MWGs. Such evanescent sources can be merely produced by the total internal reflection of 3D focused Gaussian beams on the surface of the transparent substrate on which the MWGs are deposited.<sup>19,20</sup>

In order to combine the advantages of dielectric and metallic devices, we consider hybrid systems involving high

refraction index MWGs and chains of metallic nanoparticles. In particular, we show that short linear chains of gold nanoparticles deposited on MWGs can act as a *nanometric Bragg mirror* and thus can dramatically modify the transmission spectrum of the waveguide. In a similar context, recent works have investigated ensembles of metallic nanoparticles deposited onto planar waveguides. Reference 21 first pointed out some drastic modification in the scattered light spectrum of a random array of Au nanoparticles. Inspired by this work, Linden *et al.*<sup>22</sup> recently succeeded in controlling the extinction of an ordered 2D arrangement of Au nanoparticles deposited on a planar waveguide by adjusting the pitch of the lattice. In both cases, changes occur when the fields scattered by the particles can couple with the guided modes supported by the waveguide.

The paper is organized as follows. In the next section, we use numerical simulations based on the Green's tensor formalism to compute both far-field and near-field optical spectra of composite systems made of nanoparticle chains with various periodicities deposited on different MWGs. We show that in the visible range, the transmission spectra of such hybrid systems exhibit strong modulations with the appearance of a neat band gap generated by the chain of gold particles. Inspired by these numerical results, a MWG couple to a short chain of gold nanoparticles has been microfabricated by electron beam lithography. The photon scanning tunneling microscope images of this sample are discussed in the third section. The experimental images are found to be in good qualitative agreement with computed near-field optical distributions.

## II. SIMULATIONS OF PLASMONIC CHAINS SUPPORTED BY INTEGRATED MWGs

### A. Summarizing the theoretical background

Theoretical electrodynamics modeling in the vicinity of localized objects can be performed in the framework of the field susceptibility (or Green dyadic) method.<sup>23,24</sup> Today, this method is one of the most versatile and reliable numerical techniques to solve the full set of Maxwell equations for the typical parameters of near-field optics<sup>2</sup> involving both dielectric and metallic nanostructures. This approach (called the direct space integral equation method) is based on the knowledge of the retarded dyadic tensor  $\mathbf{S}(\mathbf{r}, \mathbf{r}', \omega)$  associated with a reference system which, in our problem, is flat glass surface. The numerical procedure considers any object deposited on the surface as a localized perturbation which is discretized in direct space over a predefined volume mesh of  $N$  points  $\{\mathbf{R}_i\}$ . In a first step, the electric field distribution  $\mathbf{E}(\mathbf{R}_i, \omega)$  is determined self-consistently inside the perturbations (i.e., the source field). At this stage, a renormalization procedure associated to the depolarization effect is applied to take care of the self-interaction of each discretization cell. The final step relies on the Huygens-Fresnel principle to compute the electromagnetic field  $\mathbf{E}(\mathbf{r}, \omega)$  on the basis of the knowledge of the field inside the localized perturbations  $\mathbf{E}(\mathbf{R}_i, \omega)$ . The two main computational steps can be summarized as follows.

(i) *Local field computation inside the source field*

$$\mathbf{E}(\mathbf{R}_i, \omega) = \sum_j \mathcal{K}(\mathbf{R}_i, \mathbf{R}_j, \omega) \cdot \mathbf{E}_0(\mathbf{R}_j, \omega), \quad (1)$$

where  $\mathcal{K}$  labels the generalized field propagator of the entire system (localized object plus bare silica surface). In the  $\{\mathbf{R}_i; \mathbf{R}_j\}$  representation it is given by

$$\mathcal{K}(\mathbf{R}_i, \mathbf{R}_j, \omega) = \delta_{i,j} + v_j \mathcal{S}(\mathbf{R}_i, \mathbf{R}_j, \omega) \cdot \chi(\mathbf{R}_j, \omega), \quad (2)$$

where  $\chi$  represents the electric susceptibility of the localized object,  $v_j$  is the volume of the elementary discretization cell, and  $\mathcal{S}$  is the field susceptibility of the entire system. This last quantity is usually computed by solving Dyson's equation

$$\begin{aligned} \mathcal{S}(\mathbf{R}_i, \mathbf{R}_j, \omega) = & \mathbf{S}(\mathbf{R}_i, \mathbf{R}_j, \omega) \\ & + \sum_k v_k \mathbf{S}(\mathbf{R}_i, \mathbf{R}_k, \omega) \cdot \chi(\mathbf{R}_k, \omega) \cdot \mathcal{S}(\mathbf{R}_k, \mathbf{R}_j, \omega). \end{aligned} \quad (3)$$

(ii) *Electric and magnetic fields computation outside the source field region*

$$\mathbf{E}(\mathbf{r}, \omega) = \mathbf{E}_0(\mathbf{r}, \omega) + \sum_i v_i \mathbf{S}(\mathbf{r}, \mathbf{R}_i, \omega) \cdot \chi(\mathbf{R}_i, \omega) \cdot \mathbf{E}(\mathbf{R}_i, \omega) \quad (4)$$

and

$$\mathbf{B}(\mathbf{r}, \omega) = \mathbf{B}_0(\mathbf{r}, \omega) + \sum_i v_i \mathbf{Q}(\mathbf{r}, \mathbf{R}_i, \omega) \cdot \chi(\mathbf{R}_i, \omega) \cdot \mathbf{E}(\mathbf{R}_i, \omega). \quad (5)$$

In these two equations, the vectors  $\mathbf{E}_0(\mathbf{r}, \omega)$  and  $\mathbf{B}_0(\mathbf{r}, \omega)$  describe respectively the time Fourier transform of the electric and magnetic parts of the incident electromagnetic field. The formulas of the two Green dyadic propagators  $\mathbf{S}$  and  $\mathbf{Q}$  can be found in Ref. 25. Knowing both electric and magnetic fields outside the source field region, we can investigate either the far-field or near-field properties of arbitrary samples.

### B. Far-field spectroscopy

The model system we consider first consists in a linear chain (with a period  $a$ ) of 13 gold parallelepipeds ( $100 \times 100 \times 20 \text{ nm}^3$ ) lying on the top surface of a  $12\text{-}\mu\text{m}$ -long  $\text{TiO}_2$  wire (section  $\sigma = 200 \times 200 \text{ nm}^2$ ). The  $\text{TiO}_2$  wire is deposited itself on the surface of a glass substrate [Fig. 1(a)].

The sample is supposed to be illuminated in normal incidence by an incident electric field  $\mathbf{E}_0(\mathbf{r}, \omega)$  linearly polarized along the axis of the nanoparticle chain. This polarization direction has been chosen since it provides the stronger dipolar interaction between the particles. In order to characterize the far-field properties of this system, we compute the power scattered by the sample per unit surface with respect to the incident wavelength, according to the procedure described in Sec. II A. To perform this calculation, we use the *far-field* asymptotic form of the Green dyadic tensor  $\mathbf{S}(\mathbf{r}, \mathbf{r}', \omega)$  given in Ref. 26.

We first consider the reference situation such that the metallic nanoparticles are directly deposited at the surface of the glass substrate. The two spectra computed in absence of any

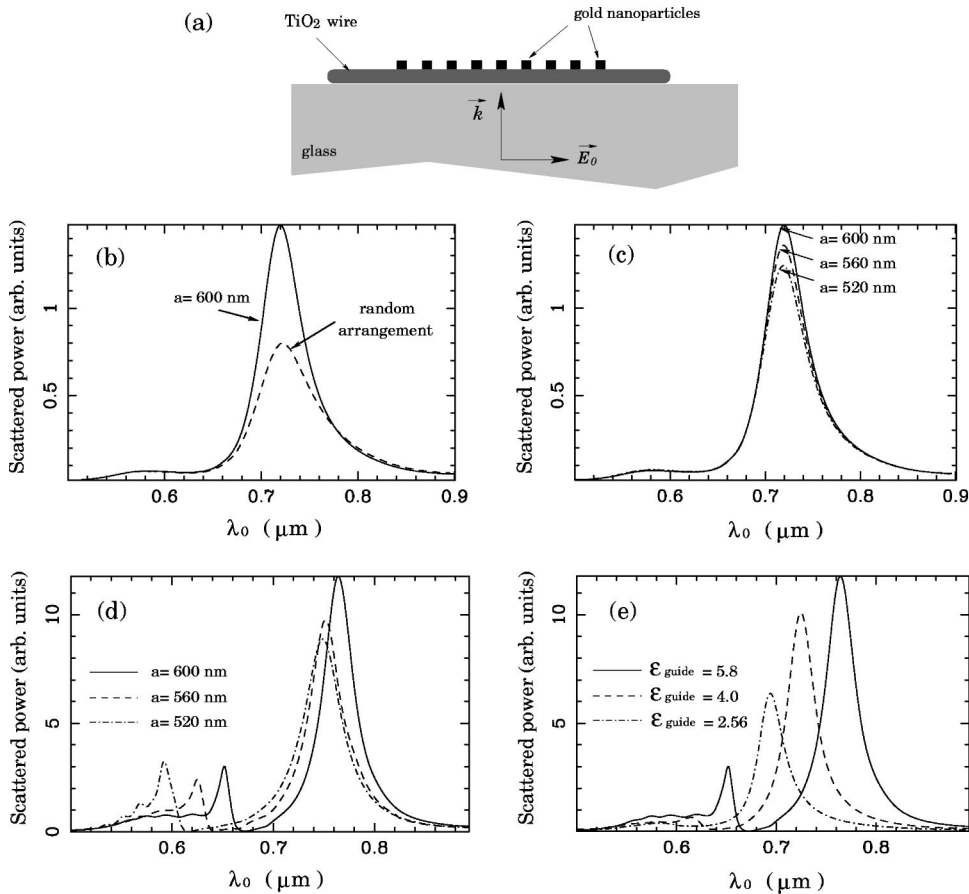


FIG. 1. Theoretical spectroscopy of the power scattered by a periodic alignment of 13 gold nanoparticles ( $100 \times 100 \times 20 \text{ nm}^3$ ). (a) Configuration of the calculation. Influence of the periodicity and of the period  $a$  when the nanoparticles are supported by a glass substrate (b) and (c) or when deposited on the top of a  $\text{TiO}_2$  wire (section  $200 \times 200 \text{ nm}^2$ , length  $12 \mu\text{m}$ ) (d). (e) Evolution of the spectrum for  $a=600 \text{ nm}$  when the dielectric function of the wire is decreased.

MWG are displayed in Figs. 1(b) and 1(c). Fig. 1(b) shows the curve obtained for a period  $a=600 \text{ nm}$ . A comparison with the spectrum of a linear random ensemble of the same number of particles illustrates how the coherent addition of the individual dipolar fields contributes to enhance, by a factor of about two, the amplitude of the plasmon resonance. The spectra computed for different values of the chain periodicity are shown in Fig. 1(c). According to these results, the value of  $a$  does not shift significantly the plasmon resonance of the particle chains when they are deposited directly on the glass substrate. Indeed, for the three values of  $a$  considered, the resonance remains centered around  $\lambda_0=720 \text{ nm}$  which corresponds to the resonance frequency of an isolated nanoparticle.

Similar calculations are repeated for complete systems of nanoparticle chains lying on MWGs. In order to make easier a direct comparison with the spectra of Figs. 1(b) and 1(c), we computed the energy radiated by the metallic nanoparticles only. Thus, the spectra shown in Figs. 1(d) and 1(e) cannot be used for comparison with experimental data since we have neglected the contribution of the MWG itself. However, this procedure offers the opportunity to demonstrate the strong influence of the MWG on the nanoparticles chains optical properties. Indeed, the spectra of Fig. 1(d) has been obtained for the chains with various periodicity deposited on  $\text{TiO}_2$  MWG with a real dielectric function of  $\epsilon_g=5.8$  supposed to be constant over the whole frequency range we consider. Two specific effects can be attributed to the presence of the MWG: (1) the LSP resonance of the particles is

significantly red-shifted compared to the previous situation (from  $720$  to  $765 \text{ nm}$  for  $a=600 \text{ nm}$ , for example). This shift originates mainly from the presence of the  $\text{TiO}_2$  material that displays a stronger dielectric constant than the glass substrate. Moreover, unlike what happens when the chain is lying on the bare substrate [see Figs. 1(b) and 1(c)], we observe now a dependence of the plasmon resonance position with respect to the interparticle distance. Note that similar effects for particles arranged to form a large 2D arrays have already been reported in both theoretical<sup>27</sup> and experimental<sup>28</sup> works. It can be understood as a consequence of the modification of the electromagnetic local field around each particle generated by the coupling between each induced dipole and their electric images in the underneath sample (here the  $\text{TiO}_2$  MWG). (2) A second consequence related to the presence of the  $\text{TiO}_2$  microwaveguide is the appearance of a second peak at higher energies. This new resonance is related to the collective response of the nanoparticles chain since its position is very sensitive to the value of  $a$ . Nevertheless, the hypothesis of a typical grating mode can be excluded as it does not appear in calculations performed in the absence of the MWG. Finally, in agreement with observations reported in Refs. 21,22, and 29, we infer these different behaviors are due to the collective coupling between the modes of the metal chains with those sustained by the microwaveguide. This statement is confirmed by the spectra displayed in Fig. 1(e). These curves have been obtained with a given value of  $a=600 \text{ nm}$  and decreasing val-

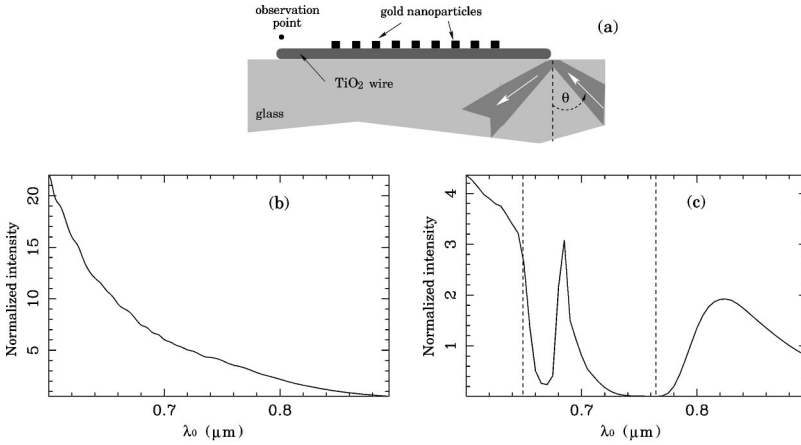


FIG. 2. (a) Geometry used for the calculation. Variation of near-field optical transmittance vs the incident wavelength (b) with a bare MWG and (c) with a MWG decorated with a gold particle chain ( $a=600$  nm). The calculation of the near-field intensity is performed 100 nm above the extremity of the wire. The dashed lines indicate the resonances observed in the far-field spectra.

ues of the MWG dielectric function. Since we keep the transverse cross section  $\sigma$  at a constant value, a decrease of the MWG dielectric function leads to a corresponding decrease of the number and/or the effective index of the guided modes. Thus, the collective coupling between the particles of the chain achieved by the guided modes of the MWG is dramatically reduced. Because the high energy peak in the far-field spectra vanishes with decreasing values of the MWG dielectric function, we can then conclude that this peak is created by the coupling between the chain modes and those of the MWG.

### C. Near-field optical transmission spectrum of the composite system

In Sec. II B, we pointed out the intricate character of the interaction between nanoparticle chains and MWGs. In this section, we wish to evaluate the role of these interactions on the near-field transmission spectra of the composite device. In order to reach this goal, we have modified the illumination configuration [see Fig. 2(a)]. The system is now locally addressed by an evanescent wave confined in the three directions whose the focus is adjusted to shine on the input end of the MWG. Such a configuration has been demonstrated, both theoretically and experimentally,<sup>30,31</sup> to be efficient for coupling with MWGs that display small cross sections.

#### 1. Homogeneous MWGs

For this first application, we have computed the electric near-field intensity  $|\mathbf{E}(\mathbf{r}_{obs}, \omega_0)|^2$  versus the incident wavelength  $\lambda_0 = 2\pi c/\omega_0$ . This near-field intensity is normalized with respect to the incident electric field intensity computed in absence of any object on the substrate at a point located in the observation plane just above the focal point of the incident focused beam. Note that because of the Goos-Hanschen shift, the normalization value we use does not correspond to the maximum intensity of the incident beam in the observation plane.<sup>30</sup> For the computation of the near-field transmission spectrum, the observation point  $\mathbf{r}_{obs}$  is represented in Fig. 2(a) and is located 100 nm above the output extremity of the MWG. The incident field is  $p$  polarized (electric field parallel to the plane of incidence), the reflection angle  $\theta$  and the beam waist are respectively  $50^\circ$  and  $1 \mu\text{m}$ . The near-

field transmission spectrum of the bare guide shown in Fig. 2(b) exhibits the expected decay when the excitation wavelength  $\lambda_0$  becomes significantly larger than the MWG average transverse size  $\sqrt{\sigma}$ .

#### 2. MWGs decorated with a linear particle chain

The near-field transmission spectrum of the composite system is shown in Fig. 2(c). The metallic chain has a dramatic influence on the transparency of the MWG. First we observe a global decrease of the transmission efficiency due to nonradiative losses of gold pads. For example the near-field intensity  $|\mathbf{E}(\mathbf{r}_{obs}, \omega_0)|^2$  is reduced by a factor of about 5 compared to the bare MWG for the wavelength  $\lambda_0 = 600$  nm. Unlike the smooth decay found in the case of the homogeneous MWG, the transmission spectrum of the composite system exhibits two pronounced attenuation bands, respectively centered on  $\lambda_0 = 666$  nm and  $\lambda_0 = 750$  nm. We note that these wavelengths match the resonances observed previously in the far-field data of Fig. 1 (dashed lines) with only small frequency shifts resulting from the difference between the two illumination configurations. Indeed, in the present application involving a local illumination of the waveguide, the electric field that propagates within the  $\text{TiO}_2$  MWG has a nonzero component along the  $z$  axis. The physical mechanisms at the origin of the photonic band gap in the spectrum of Fig. 2(c) involve (i) phase effects (as in a usual Bragg mirror), (ii) radiative coupling of the metal chain with the vacuum electromagnetic states, and (iii) nonradiative losses inside the metal particle. Thus, in our case, the decrease in the transparency is mainly associated with a strong coupling of the field propagating in the  $\text{TiO}_2$  core with the modes of the gold chain that induce important radiative and non-radiative signal losses for frequencies close to the resonances of the metallic chain.

Additionally, the two transmission gaps in Fig. 2(c) give rise to a quite narrow transparent window a full width at half maximum of 15 nm, centered on  $\lambda_0 = 685$  nm. The possibility of controlling its position and its width by changing the structural parameters of the metal pattern (periodicity, number of particles, particles geometry) could find potential applications for selective filtering. To close our numerical analysis, in Fig. 3 we present three electric near-field intensity maps computed above the composite system in an ob-

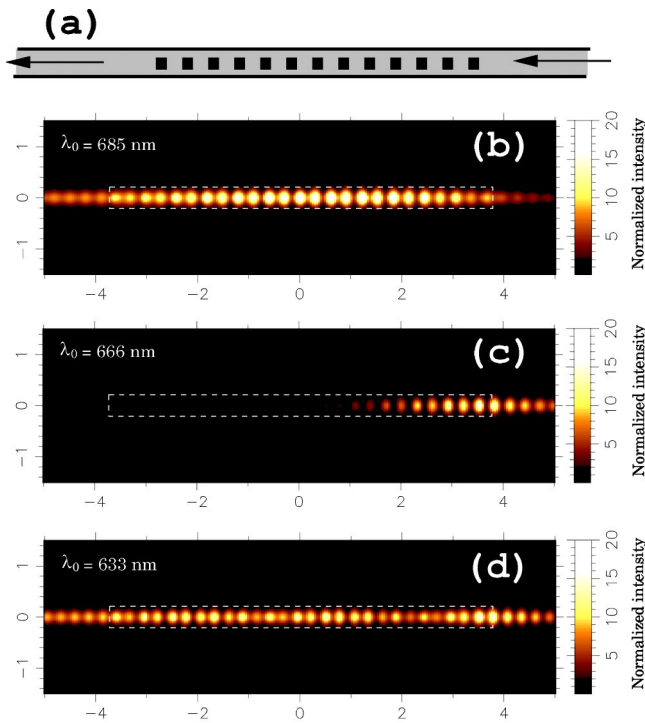


FIG. 3. (a) Top view of the computational situation (longitudinal axis: OY). (b)–(d) Electric near-field intensity maps calculated over the composite system for three different incident wavelengths. The dashed line frame shows the location of the metallic chain.

servation plane parallel located at a distance of 100 nm over the top surface of the MWG. The calculations have been made for three wavelengths corresponding to three different transmission regimes. For  $\lambda_0=666$  nm, the intensity dramatically decreases along the two first micrometers where the chain is located. In this frequency range, no significant signal is transmitted at the output extremity. Note that a similar behavior have been numerically reproduced within the larger stopping band centered around  $\lambda_0=750$  nm (not shown). Around the frequencies  $\lambda_0=685$  and 633 nm, an efficient signal transfer regime is reached. It gives rise to strong and regular near-field patterns that cover all the device. Despite the strong scattering occurring around the gold particles, the optical near-field remains well confined along the MWG. To conclude this section, let us emphasize that such numerical investigations of the optical near-field properties only require a specification of the frequency dependent dielectric constant and the shape of the lithographically designed nanostructures. Consequently, many other chain geometries (particles sizes and spacings) and plasmonic materials could be investigated with this technique, leading thereby to the prediction of the stop-band location associated with other selected geometries. Such additional information is left for a forthcoming more technical paper.

#### D. Influence of the incident light polarization on the MWG coupling

Usually, the images recorded with a near-field optical microscope reveal dramatic changes when passing from the  $p$

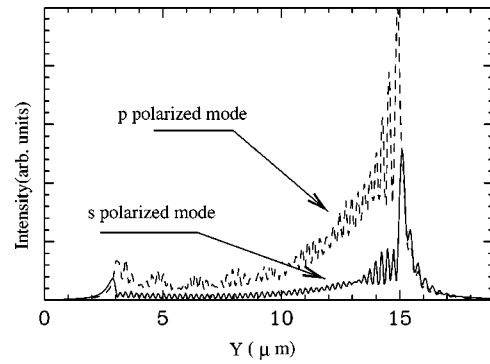


FIG. 4. Two cross sections of the electric near-field intensity computed along the main axis (OY) of a bare MWG for two different polarizations. The incident wavelength is  $\lambda_0=633$  nm and the calculation has been performed over the entire device and 75 nm above the top face of the MWG.

polarization (also called TM for transverse magnetic) to the  $s$  polarization (the so-called TE polarization for transverse electric polarization). The terms TM and TE refer the magnetic or electric light-field vector polarized transverse to the plane of incidence. In general, TM-polarized light tends to display larger contrast than TE-polarized light.<sup>32</sup> A comparative analysis of the near-field optical response of a bare MWG to the main polarizations  $s$  and  $p$  is given in Fig. 4 for a wavelength belonging to the transmission frequency located around  $\lambda_0=633$  nm. It may be seen that, like what happens in near-field optical imaging, the  $p$  polarized mode leads to a better transmission level of the device. Consequently, this operating mode should be preferred in all further experimental studies.

### III. EXPERIMENTAL RESULTS

In this section, we present preliminary optical measurements of the influence of gold nanoparticles on the near-field transmission of a TiO<sub>2</sub> MWG. The microfabricated structure consists of a 50- $\mu$ m long, 600-nm-wide, and 150-nm-high TiO<sub>2</sub> wire lying on a glass substrate. Onto its top surface, 13 gold nanoparticles (diameter  $100\pm 20$  nm, height  $20\pm 3$  nm) are regularly aligned ( $a=550\pm 20$  nm) (Fig. 5).

#### A. Microfabrication process

The fabrication process consists in a two step  $e$ -beam lithography process combined with dry etching. We started

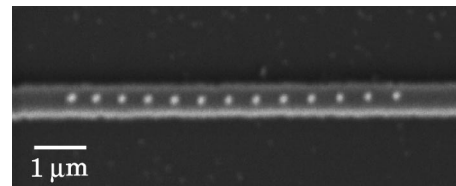


FIG. 5. Scanning electron microscope image of the microfabricated structured MWG. The TiO<sub>2</sub> wire is  $600\pm 20$  nm wide, 150 nm high, and 50  $\mu$ m long. The metallic chain consists in 13 gold nanoparticles (diameter  $100\pm 20$  nm, height=20 nm) periodically arranged ( $a=550\pm 20$  nm).

from a 150-nm-thick  $\text{TiO}_2$  ( $n_{\text{TiO}_2} = 2.41$ ) layer deposited by assisted ion beam deposition onto a glass BK7 substrate. First, the  $e$ -beam patterning of the host  $\text{TiO}_2$  wire was performed by a SEM microscope JEOL 840-A operating at 20 keV on a layer of polymethylmethacrylate (PMMA) resist ( $950 \times 10^3$  molecular weight and 150-nm thickness). After development of the PMMA film, a 40-nm nickel coating is evaporated by  $e$ -beam deposition and lifted off by dissolution of the PMMA. Reactive ion etching is then performed in a GIR 300 ALCATEL system. The etching process uses a  $\text{SF}_6(5/6)/\text{Ar}(1/6)$  equal flow rate gas mixture at a pressure of 0.015 mbar and rf power of 40 W. Then, the remaining Ni mask is removed in nitrite acid solution. The patterning of the gold nanoparticles requires a second  $e$ -beam lithography operation. At this stage, the main difficulty is a precise positioning of the sample required for the particles to be aligned along the microwire. Considering the specificities of our SEM microscope, a satisfying alignment has only been attained for wires with widths greater or equal to 600 nm.

### B. Photon scanning tunneling microscopy of the guiding structure

The optical characterization of the microfabricated structure was performed by a photon scanning tunneling microscope (PSTM).<sup>33–35</sup> An optical fiber is piezoelectrically driven so as to act as local probe of the optical field in the near-field zone.<sup>36</sup> The probes we used have been coated with 7 nm of Cr in order to reduce the contribution of scattered radiative fields in the detection process. In our experiments the PSTM probe was scanned at a constant height. In this configuration, the signal detected is well known to be related to the spatial distribution of the intensity of the local electric field. The waveguide is locally excited, as in Fig. 2(a), by a focused laser beam which is totally reflected at the substrate interface. This local illumination is produced by injecting a laser beam in a lensed single mode optical fiber (numerical aperture=0.17, working distance=18 mm). Since the data of Fig. 4 indicate a more efficient coupling with  $p$  polarized incident light, we have used this polarization mode in our experimental investigations. Moreover, by choosing the reflection angle around  $50^\circ$ , the resulting evanescent light spot at the glass-air interface features an elliptic shape with a long axis of  $12 \mu\text{m}$  (along the incident direction) and a short axis of  $8 \mu\text{m}$ .<sup>20</sup> PSTM images of bare MWG's show up near-field patterns similar to those previously described in Ref. 31. When decorated with a gold nanoparticle chain, PSTM imaging reveals dramatic changes with respect to the incident wavelength. Figure 6 displays two PSTM images recorded above the structure of Fig. 5, for two different incident wavelengths  $\lambda = 633 \text{ nm}$  and  $\lambda = 543 \text{ nm}$ , respectively. In both images, the dashed line frame indicates the area of the  $\text{TiO}_2$  MWG which is textured by the gold nanoparticles. For both wavelengths, the distribution of the electric intensity before the structured zone ( $y > 2.8 \mu\text{m}$ ) exhibits a periodic pattern, with periods of about  $650 \text{ nm}$  for  $\lambda = 543 \text{ nm}$  and about  $1 \mu\text{m}$  for  $\lambda = 633 \text{ nm}$ . These beatings result from the excitation of several modes propagating within the waveguide. Because of our current memory limitations, no com-

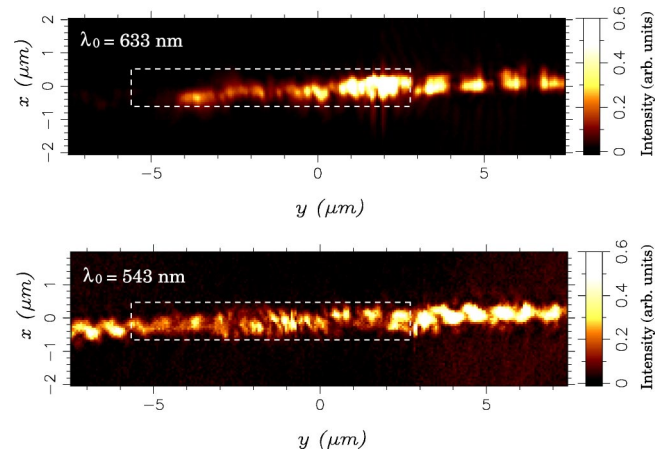


FIG. 6. PSTM images recorded less than 50 nm over the heterostructure for two different wavelengths,  $\lambda_0 = 633$  and  $543 \text{ nm}$ . The dashed line frame labels the zone occupied by the particles.

puterized simulation has been performed for the sizes of the microfabricated structure. Nevertheless, considering the results of Ref. 31, the transmission spectrum is expected more complicated than for a 200-nm-wide MWG. Indeed, for a multimode host waveguide, the coupling with the particles is distinct for each guided modes and should thus give rise to additional attenuations. For  $\lambda_0 = 633 \text{ nm}$ , the near-field intensity dramatically decreases over the first micrometers of the structured part and only a negligible part of the signal is transmitted beyond this zone. This behavior is very similar to what occurs in the simulation for  $\lambda_0 = 666 \text{ nm}$ . In that sense, despite the geometrical differences with the structure considered in the calculations, this low transmission can be attributed to one of the transmission gap predicted by the spectrum of Fig. 2(c). The damping of the electric intensity is much less pronounced for  $\lambda_0 = 543 \text{ nm}$ ; a significant part of the incident field is transmitted. For this wavelength, the nanoparticle chain is off resonance and acts as a weakly absorbing defect.

### IV. CONCLUSION AND OUTLOOK

We have shown in this work that a periodic arrangement of gold nanoparticles can strongly modify the transmission of a dielectric MWG. Simulations based on the Green dyadic method have revealed an intricate interaction between the LSP modes sustained by the particles and the guided modes underneath. These interactions give rise to strong resonances in the scattering spectrum of the metallic pattern. Calculations of the near-field transmission of the structured wire indicate that these resonances are directly correlated with the appearance of pronounced attenuations in the transmitted signal. Optical near-field measurements, performed with a PSTM, have allowed two transmission regimes (on and off) to be observed in the vicinity of the device.

This kind of heterostructure could stimulate promising applications in the domain of integrated optics, especially for

the realization of compact linear filters. With these aims in mind, the next step could be to investigate the respective influence of the different parameters (particle geometry, constitutive metal, and waveguide dispersion) in order to be able

to tailor precisely the transparency of the host MWG. Finally, the patterning of the nanoparticles could be made easier by a local deposition of the metal based on a focused ion beam technique.

- <sup>1</sup>W.L. Barnes, A. Dereux, and T.W. Ebbesen, *Nature (London)* **424**, 824 (2003).
- <sup>2</sup>J. Weeber, A. Dereux, C. Girard, J.R. Krenn, and J.P. Goudonnet, *Phys. Rev. B* **60**, 9061 (1999).
- <sup>3</sup>P. Berini, *Phys. Rev. B* **61**, 10 484 (2000).
- <sup>4</sup>R. Charbonneau, P. Berini, E. Berolo, and E. Lisicka-Shrzek, *Opt. Lett.* **25**, 844 (2000).
- <sup>5</sup>B. Lamprecht, J.R. Krenn, G. Schider, H. Ditlbacher, M. Salerno, N. Felidj, A. Leitner, and F.R. Aussenegg, *Appl. Phys. Lett.* **79**, 51 (2001).
- <sup>6</sup>J.C. Weeber, J.R. Krenn, A. Dereux, B. Lamprecht, Y. Lacroute, and J.P. Goudonnet, *Phys. Rev. B* **64**, 045411 (2001).
- <sup>7</sup>J. Takahara, S. Yamagishi, H. Taki, A. Morimoto, and T. Kobayashi, *Appl. Phys. Lett.* **22**, 475 (1997).
- <sup>8</sup>J.R. Krenn, B. Lamprecht, H. Ditlbacher, G. Schider, M. Salerno, A. Leitner, and F.R. Aussenegg, *Europhys. Lett.* **60**, 663 (2002).
- <sup>9</sup>J.R. Krenn, A. Dereux, J.C. Weeber, E. Bourillot, Y. Lacroute, J.P. Goudonnet, G. Schider, W. Gotschy, A. Leitner, F.R. Aussenegg, and C. Girard, *Phys. Rev. Lett.* **82**, 2590 (1999).
- <sup>10</sup>S.A. Maier, M.L. Brongersma, P.G. Kik, and H.A. Atwater, *Phys. Rev. B* **65**, 193408 (2002).
- <sup>11</sup>M.L. Brongersma, J.W. Hartman, and H.A. Atwater, *Phys. Rev. B* **62**, R16 356 (2000).
- <sup>12</sup>C. Bohren and D. Huffman, *Absorption and Scattering of Light by Small Particles* (Wiley, New York, 1983).
- <sup>13</sup>K. Drexhage, *Prog. Opt.* **XII**, 163 (1974).
- <sup>14</sup>W.R. Holland and D.G. Hall, *Phys. Rev. Lett.* **52**, 1041 (1984).
- <sup>15</sup>M. Quinten, A. Leitner, J.R. Krenn, and F.R. Aussenegg, *Opt. Lett.* **23**, 1331 (1998).
- <sup>16</sup>S.A. Maier, P.G. Kik, H.A. Atwater, S. Meltzer, E. Harel, B.E. Koel, and A. Requicha, *Nat. Mater.* **2**, 229 (2003).
- <sup>17</sup>S.C. Kitson, W.L. Barnes, and J.R. Sambles, *Phys. Rev. Lett.* **77**, 2671 (1996).
- <sup>18</sup>S.I. Bozhevolnyi, J. Erland, K. Leosson, P. Skovgaard, and J. Hvam, *Phys. Rev. Lett.* **86**, 3009 (2001).
- <sup>19</sup>R. Quidant, J.C. Weeber, A. Dereux, D. Peyrade, C. Girard, and Y. Chen, *Phys. Rev. E* **65**, 036616 (2002).
- <sup>20</sup>R. Quidant, J.C. Weeber, A. Dereux, D. Peyrade, Y. Chen, and C. Girard, *Europhys. Lett.* **65**, 191 (2002).
- <sup>21</sup>H.R. Stuart and D.G. Hall, *Phys. Rev. Lett.* **80**, 5663 (1998).
- <sup>22</sup>S. Linden, J. Kuhl, and H. Giessen, *Phys. Rev. Lett.* **86**, 4688 (2001).
- <sup>23</sup>O.J.F. Martin, C. Girard, and A. Dereux, *Phys. Rev. Lett.* **74**, 526 (1995).
- <sup>24</sup>J.-J. Greffet and R. Carminati, *Prog. Surf. Sci.* **56**, 133 (1997).
- <sup>25</sup>C. Girard, J.C. Weeber, A. Dereux, O.J. Martin, and J.P. Goudonnet, *Phys. Rev. B* **55**, 16 487 (1997).
- <sup>26</sup>A. Dereux, Ph.D. thesis, Facultés Universitaires Notre-Dame de la Paix, Namur, Belgium, 1991.
- <sup>27</sup>M. Meier, A. Wokaum, and P.F. Liao, *J. Opt. Soc. Am. B* **2**, 931 (1985).
- <sup>28</sup>B. Lamprecht, B. Lamprecht, G. Schider, R.T. Lechner, H. Ditlbacher, J.R. Krenn, A. Leitner, and F.R. Aussenegg, *Phys. Rev. Lett.* **84**, 4721 (2000).
- <sup>29</sup>B. Soller and D.G. Hall, *J. Opt. Soc. Am. B* **19**, 1195 (2002).
- <sup>30</sup>J.C. Weeber, A. Dereux, C. Girard, G. Colas-des-Francis, J.R. Krenn, and J.P. Goudonnet, *Phys. Rev. E* **62**, 7381 (2000).
- <sup>31</sup>R. Quidant, R. Quidant, J.C. Weeber, A. Dereux, D. Peyrade, G. Colas-des-francis, and C. Girard, *Phys. Rev. E* **64**, 066607 (2001).
- <sup>32</sup>K. Propstra and N.K.V. Hulst, *J. Microsc.* **180**, 165 (1995).
- <sup>33</sup>R.C. Reddick, R.J. Warmack, and T.L. Ferrell, *Phys. Rev. B* **39**, 767 (1989).
- <sup>34</sup>R.C. Reddick, R.C. Reddick, R.J. Warmack, D.W. Chilcott, S.L. Sharp, and T.L. Ferrell, *Rev. Sci. Instrum.* **61**, 3669 (1990).
- <sup>35</sup>D. Courjon, K. Sarayedine, and M. Spajer, *Opt. Commun.* **71**, 23 (1989).
- <sup>36</sup>A. Dereux, C. Girard, and J. Weeber, *J. Chem. Phys.* **112**, 7775 (2000).